Vision, Modeling, and Visualization (2013)
Michael Bronstein, Jean Favre, and Kai Hormann (Eds.)

Datasets and Benchmarks for Densely Sampled 4D Light Fields

Sven Wanner, Stephan Meister and Bastian Goldluecke

Heidelberg Collaboratory for Image Processing

Abstract

We present a new benchmark database to compare and evaluate existing and upcoming algorithms which are tailored to light field processing. The data is characterised by a dense sampling of the light fields, which best fits current plenoptic cameras and is a characteristic property not found in current multi-view stereo benchmarks. It allows to treat the disparity space as a continuous space, and enables algorithms based on epipolar plane image analysis without having to refocus first. All datasets provide ground truth depth for at least the center view, while some have additional segmentation data available. Part of the light fields are computer graphics generated, the rest are acquired with a gantry, with ground truth depth established by a previous scanning of the imaged objects using a structured light scanner. In addition, we provide source code for an extensive evaluation of a number of previously published stereo, epipolar plane image analysis and segmentation algorithms on the database.

1. Introduction

The concept of a light field was originally used mainly in computer graphics as a powerful tool to describe scene appearance [AB91, LH96], but recently it is also getting more and more attention from the computer vision community. One of the likely reasons is the availability of cheap recording devices. While the first light field capturing techniques used large camera arrays [WJV*05] which are expensive and not very practicable, hand-held light field cameras [Ng06, PW10] are now available on the consumer market.

However, the driving force for successful algorithm development is the availability of suitable benchmark datasets with ground truth data in order to compare results and initiate competition. The current public light field databases we are aware of are the following.

- **Stanford Light Field Archive**
  http://lightfield.stanford.edu/lfs.html
  The Stanford Archives provide more than 20 light fields sampled using a camera array [WJV*05], a gantry and a light field microscope [LNA*06], but none of the datasets includes ground truth disparities.
- **UCSD/MERL Light Field Repository**
  http://vision.ucsd.edu/datasets/lfarchive/lfs.shtml
  This light field repository offers video as well as static light fields, but there is also no ground truth depth available, and the light fields are sampled in a one-dimensional domain of view points only.
- **Synthetic Light Field Archive**
  http://web.media.mit.edu/~gordonw/SyntheticLightFields/index.php
  The synthetic light field archive provides many interesting artificial light fields including some nice challenges like transparencies, occlusions and reflections. Unfortunately, there is also no ground truth depth data available for benchmarking.
- **Middlebury Stereo Datasets**
  http://vision.middlebury.edu/stereo/data/
  The Middlebury Stereo Dataset includes a single 4D light field which provides ground truth data for the center view, as well as some additional 3D light fields including depth information for two out of seven views. The main issue with the Middlebury light fields are that they are designed with stereo matching in mind, and thus the baselines are quite large and thus not representative for plenoptic cameras and unsuitable for direct epipolar plane image analysis.

While there is a lot of variety and the data is of high quality, we observe that all of the available light field databases either lack ground truth disparity information or exhibit large camera baselines and disparities, which is not representative for plenoptic camera data. Furthermore, we believe that a

large part of what distinguishes light fields from standard multi-view images is the ability to treat the view point space as a continuous domain. There is also emerging interest in light field segmentation [KSS12, SHH07, EM03, WSG13], so it would be highly useful to have ground truth segmentation data avaliable to compare light field labeling schemes. The above datasets lack this information as well.

Contributions. To alleviate the above shortcomings, we present a new benchmark database which consists at the moment of 13 high quality densely sampled light fields. The database offers seven computer graphics generated datasets providing complete ground truth disparity for all views. Four of these datasets also come with ground truth segmentation information and pre-computed local labeling cost functions to compare global light field labeling schemes. Furthermore, there are six real world datasets captured using a single Nikon D800 camera mounted on a gantry. Using this device, we sampled objects which were pre-scanned with a structured light scanner to provide ground truth ranges for the center view. An interesting special dataset contains a transparent surface with ground truth disparity for both the surface as well as the object behind it - we believe it is the first real-world dataset of this kind with ground truth depth available.

We also contribute a CUDA C library with complete source code for several recently published algorithms to demonstrate a fully scripted evaluation on the benchmark database and find an initial ranking of a small subset of the available methods on disparity estimation. We hope that this will ease the entry into the interesting research area which is light field analysis, and are fully commited to increasing the scope of the library in the future.

2. The light field archive

Our light field archive (`www.lightfield-analysis.net`) is split into two main categories, *Blender* and *Gantry*. The Blender category consists of seven scenes rendered using the open source software Blender [Ble] and our own light field plugin, see figure 2 for an overview of the datasets. The Gantry category provides six real-world light fields captured with a commercially available standard camera mounted on a gantry device, see figure 5. More information about all the datasets can be found in the overview in figure 1.

Each dataset is split into different files in the HDF5-format [The10], exactly which of these are present depends on the available information. Common to all datasets is a main file called **lf.h5**, which contains the light field itself and the range data. In the following, we will explain its content as well as that of the different additional files, which can be specific to the category.

dataset name	category	resolution	GTD	GTL
buddha	Blender	768x768x3	full	yes
horses	Blender	576x1024x3	full	yes
papillon	Blender	768x768x3	full	yes
stillLife	Blender	768x768x3	full	yes
buddha2	Blender	768x768x3	full	no
medieval	Blender	720x1024x3	full	no
monasRoom	Blender	768x768x3	full	no
couple	Gantry	898x898x3	cv	no
cube	Gantry	898x898x3	cv	no
maria	Gantry	926x926x3	cv	no
pyramide	Gantry	898x898x3	cv	no
statue	Gantry	898x898x3	cv	no
transparency	Gantry	926x926x3	2xcv	no

Figure 1: Overview of the datasets in the benchmark. ***dataset name****: The name of the dataset.* ***category****: Blender (rendered synthetic dataset) or Gantry (real-world dataset sampled using a single moving camera).* ***resolution****: spatial resolution of the views, all light fields consist of 9x9 views.* ***GTD****: indicates completeness of ground truth depth data, either cv (only center view) or full (all views). A special case is the transparency dataset, which contains ground truth depth for both background and transparent surface.* ***GTL****: indicates if object segmentation data is available.*

2.1. The main file

The main file **lf.h5** for each scene consists of the actual light field image data as well as the ground truth depth, see figure 1. Each light field is 4D, and sampled on a regular grid. All images have the same size, and views are spaced equidistantly in horizontal and vertical direction, respectively. The general properties of the light field can be accessed in the following attributes:

HDF5 attribute	description
yRes	height of the images in pixel
xRes	width of the images in pixel
vRes	# of images in vertical direction
hRes	# of images horizontal direction
channels	light field is rgb (3) or grayscale (1)
vSampling	rel. camera position grid vertical
hSampling	rel. camera position grid horizontal

The actual data is contained in two HDF5 datasets:

HDF5 dataset	size
LF	*vRes* x *hRes* x *xRes* x *yRes* x *channels*
GT_DEPTH	*vRes* x *hRes* x *xRes* x *yRes*

These store the separate images in RGB or grayscale (range 0-255), as well as the associated depth maps, respectively.

Conversion between depth and disparity. To compare disparity results to the ground truth depth, the latter has to first be converted to disparity. Given a depth Z, the disparity

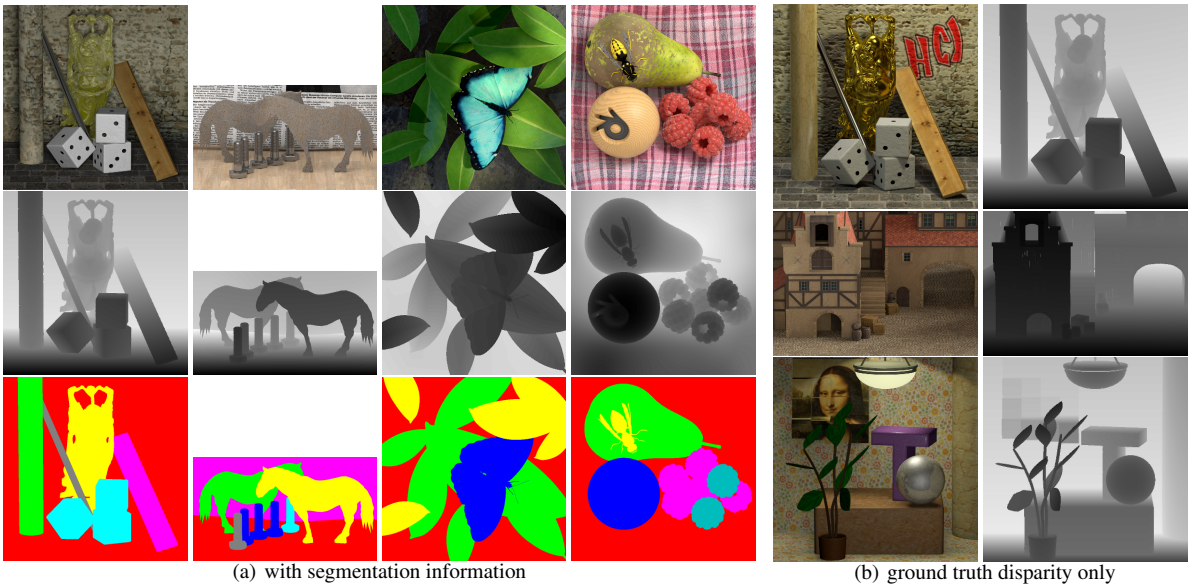

(a) with segmentation information (b) ground truth disparity only

Figure 2: *Datasets in the category Blender. (a) Light fields with segmentation information available. From left to right: buddha, horses, papillon, stillLife, top to bottom: center view, depth map, labeling. (b) Light fields without segmentation information. From top to bottom: buddha2, medieval, monasRoom, left to right: center view, depth map.*

or slope of the epipolar lines d in pixels per grid unit is

$$d = \frac{B * f}{Z} - \Delta x, \tag{1}$$

where B is the baseline or distance between two cameras, f the focal length in pixel and Δx the shift between two neighbouring images relative to an arbitrary rectification plane (in case of light fields generated with Blender, this is the scene origin). The parameters in equation 1 are given by the following attributes in the main HDF file:

	attribute	description
B	*dH*	distance between to cameras
f	*focalLength*	focal length
Δx	*shift*	shift between neighbouring images

The following subsections describe differences and conventions about the depth scale for the two current categories.

2.2. Blender category

The computer graphics generated scenes consist without exception of ground truth depth over the entire light field. This information is given as orthogonal distance of the 3D point to the image plane of the camera, measured in Blender units $[BE]$. The Blender main files have an additional attribute *camDistance* which is the base distance of the camera to the origin of the 3D scene, and used for the conversion to disparity values.

Conversion between Blender depth units and disparity. The above HDF5 camera attributes in the main file for conversion from Blender depth units to disparity are calculated from Blender parameters via

$$\begin{aligned} dH &= b * xRes, \\ focalLength &= 1/\left(2 * tan\left(\frac{fov}{2}\right)\right), \\ shift &= \frac{1}{\left(2 * Z_0 * tan\left(\frac{fov}{2}\right)\right) * b}, \end{aligned} \tag{2}$$

where Z_0 is the distance between the blender camera and the scene origin in $[BE]$, fov is the field of view in units radian and b the distance between two cameras in $[BE]$. Since all light fields are rendered or captured on a regular equidistant grid, it is sufficient to use only the horizontal distance between two cameras to define the baseline.

2.2.1. Segmentation ground truth

Some light fields have segmentation ground truth data available, see figure 1, and offer five additional HDF5 files:

- **labels.h5**:
  This file contains the HDF5 dataset *GT_LABELS* which is the segmentation ground truth for all views of the light field and the HDF5 dataset *SCRIBBLES* which are user scribbles on a single view.
- **edge_weights.h5**:
  Contains a HDF5 dataset called *EDGE_WEIGHTS* which

are probabilities for edges [WSG13] for all views. These are not only useful for segmentation, but any algorithm which might require edge information, and can help with comparability since all of these can use the same reference edge weights.

- **feature_single_view_probabilities.h5**:
  The HDF5 dataset *Probabilities* contains the prediction of a random forest classifier trained on a single view of the light field without using any feature requiring light field information [WSG13].
- **feature_depth_probabilities.h5**:
  The HDF5 dataset *Probabilities* contains the prediction of a random forest classifier trained on a single view of the light field using estimated disparity [WG12] as an additional feature [WSG13].
- **feature_gt_depth_probabilities.h5**:
  The HDF5 dataset *Probabilities* contains the prediction of a random forest classifier trained on a single view of the light field using ground truth disparity as an additional feature [WSG13].

2.3. Gantry category

In the Gantry category, each scene always provides a single main **lf.h5** file, which contains an additional HDF5 dataset *GT_DEPTH_MASK*. This is a binary mask indicating valid regions in the ground truth *GT_DEPTH*. Invalid regions in the ground truth disparity have mainly two causes. First, there might be objects in the scene for which no 3D data is available, and second, there are parts of the mesh not covered by the structured light scan and thus having unknown geometry. See section 3.2.1 for details.

A special case is the light field *transparency*, which has two depth channels for a transparent surface and an object behind it, respectively. Therefore, there also exist two mask HDF5 datasets, see figure 3. We believe this is the first benchmark light field for multi-channel disparity estimation. Here, the HDF5 datasets are named

- *GT_DEPTH_FOREGROUND*,
- *GT_DEPTH_BACKGROUND*,
- *GT_DEPTH_FOREGROUND_MASK*,
- *GT_DEPTH_BACKGROUND_MASK*.

3. Generation of the light fields

The process of light field sampling is very similar for both the synthetic as well as the real world scenes. The camera is moved on a equidistant grid parallel to its own sensor plane and an image is taken at each grid position. Although not strictly necessary, an odd number of grid positions is used for each movement direction as there then exists a well-defined center view which makes the processing simpler. An epipolar rectification on all images is performed to align individual views to the center one. The source for the internal and external camera matrices needed for this rectification depends on the capturing system used.

Figure 3: *Dataset transparency. Top: center view, bottom left: depth of the background, bottom right: depth of the foreground.*

3.1. Blender category

For the synthetic scenes, the camera can be moved using a script for the Blender engine. As camera parameters can be set arbitrarily and the sensor and movement plane coincide perfectly, no explicit camera calibration is necessary. Instead, the values required for rectification can be derived directly from the internal Blender settings.

3.2. Gantry category

For the real-world light fields, a Nikon D800 digital camera is mounted on a stepper-motor driven gantry manufactured by Physical Instruments. A picture of the setup can be seen in figure 4. Accuracy and repositioning error of the gantry is well in the micrometer range. The capturing time for a complete light field depends on the number of images, about 15 seconds are required per image. As a consequence, this acquisition method is limited to static scenes. The internal camera matrix must be estimated beforehand by capturing images of a calibration pattern and invoking the camera calibration algorithms of the OpenCV library, see next section

Figure 4: *Picture of the gantry setup showing a sample object placed on the left and the camera mounted on a stepper-motor on the right.*

for details. Experiments have shown that the positioning accuracy of the gantry actually surpasses the pattern based external calibration as long as the differences between the sensor and movement planes are kept minimal.

3.2.1. Ground truth for the Gantry light fields

Ground truth for the real world scenes was generated using standard pose estimation techniques. First, we acquired 3D polygon meshes for an object in the scene using a Breuckmann SmartscanHE structured light scanner. The meshes contain between 2.5 and 8 Million faces with a stated accuracy of down to 50 micron. The object-to-camera pose was estimated by hand-picking 2D-to-3D feature points from the light field center view and the 3D mesh, and then calculating the external camera matrix using an iterative Levenberg-Marquardt approach from the OpenCV library [Bra00]. This method is used for both the internal and external calibration. An example set of correspondence points for the scene *pyramide* can be observed in figure 6.

The reprojection error for all scenes was typically 0.5 ± 0.1 pixels. The depth is then defined as the distance between the sensor plane and the mesh surface visible in each pixel. The depth projections are computed by importing the mesh and measured camera parameters into Blender and performing a depth rendering pass. At depth discontinuities (edges) or due to the fact that the meshes' point density is higher than the lateral resolution of the camera, one pixel can contain multiple depth cues. In the former case, the pixel was masked out as an invalid edge pixel and in the latter case, the depth of the polygon with the biggest area inside the pixel was selected. The error is generally negligible as the geometry of the objects is sufficiently smooth at these scales. Smaller regions where the mesh contained holes were also masked out and not considered for the final evaluations.

For an accuracy estimation of the acquired ground truth,

Figure 5: *Datasets in the category Gantry. From left to right: center view, depth channel, mask which indicates regions with valid depth information. The ordering of the datasets is the same as in figure 1.*

we perform a simple error propagation on the projected point coordinates. Given an internal camera matrix C and an external matrix R, a 3D point $\vec{P} = (X, Y, Z, 1)$ is projected onto the sensor pixel $(u\ v)$ according to

$$\begin{pmatrix} u \\ v \\ 1 \end{pmatrix} = C\,R \begin{pmatrix} X \\ Y \\ Z \\ 1 \end{pmatrix}.$$

For simplicity, we assume that the camera and object coordinate systems coincide, save for an offset t_z along the optical axis. Given focal length f_x, principal point c_x and reprojection error Δu, this yields for a pixel on the $v = 0$ scanline

$$t_z = Z - \frac{f_x X}{u - c_x},$$

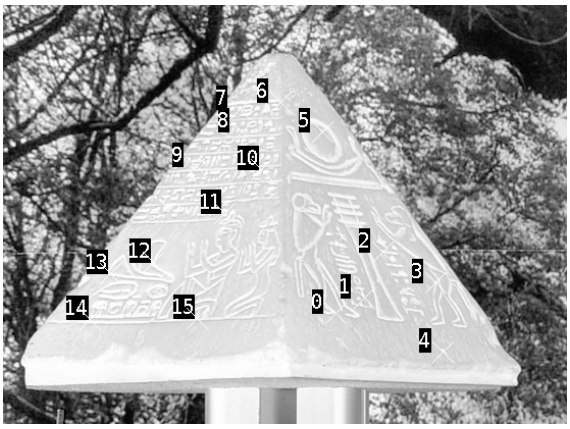

Figure 6: *Selected 2D correspondences for pose estimation for the pyramide dataset. In theory, four points are sufficient to estimate the six degrees of freedom of an external camera calibration matrix, but more points increase the accuracy in case of outliers.*

resulting in a depth error Δt_z of

$$\Delta t_z = \frac{\partial t_z}{\partial u}\Delta u = \frac{f_x X}{(c_x - u)^2}\Delta u.$$

Calculations for pixels outside of the center scanline are performed analogously. The error estimate above depends on the distance of the pixel from the camera's principal point. As the observed objects are rigid, we assume that the distance error Δt_z between camera and object corresponds to the minimum observed Δt_z among the selected 2D-3D correspondences. For all gantry scenes, this value is in the range of $1mm$ so we assume this to be the approximate accuracy of our ground truth.

4. Evaluation

The benchmark data sets are accompanied by a test suite which is coded in CUDA / C++ and which contains a number of implementations for recent light field analysis algorithms. Complete source code is available, and it is our intention to improve and update the test suite over the next years. As such, the list of algorithms and results below is only a snapshot of the current implementation. For example, an implementation of the multiview graph cut scene reconstruction [KZ02] is scheduled for an upcoming version. We will regularly publish benchmark results for the newest implementation.

The project will be hosted on SourceForge, and others are of course invited to contribute more algorithms for comparison and evaluation, but this is not a requirement to get listed in the results. Instead, we will provide a method independent from the test suite code to submit results and have them ranked in the respective tables.

Algorithm	accuracy	speed	all views
ST_CH_G	1.01	slow	
EPI_C	1.04	medium	yes
EPI_S	1.07	fast	yes
ST_AV_G	1.12	slow	
ST_CH_S	1.14	fast	
EPI_G	1.18	slow	
ST_AV_S	1.19	fast	
EPI_L	1.64	fast	yes
ST_AV_L	2.72	fast	
ST_CH_L	3.54	fast	

Figure 8: *Algorithms ranked by average accuracy over all data sets (mean squared error times 100). The computation time depends on exact parameter settings and can vary quite a bit, so we have only roughly classified the algorithms as* fast *(less than five seconds),* medium *(five seconds to a minute) and* slow *(more than a minute). The column* all views *indicates whether the algorithm computes the disparity for all views of the light field in the given time frame or only for the center view.*

4.1. Disparity reconstruction algorithms

The following is a description of the methods for disparity reconstruction which are currently implemented in the test suite and ranked in the results. See figure 8 for an overview, and figure 7 for detailed results.

For all methods, we compute results from local data terms separately, and compared the same regularization schemes where possible. In the test suite, many more regularization schemes are implemented and are ready to use. However, comparisons are restricted to a subset of simple regularizers, since usually the data term has more influence on the quality of the result.

4.1.1. EPI-based methods

A number of methods exist which estimate disparity by computing the orientation of line patterns on the epipolar plane images [BBM87, CKS*05, WG12]. They make use of the well known fact that a 3D point is projected onto a line whose slope is related to the distance of the point to the observer.

For the benchmark suite, we implemented a number of schemes of varying complexity. First, we start with the purely local method **EPI_L**, which estimates orientation using an Eigensystem analysis of the structure tensor [WG12]. The second method, **EPI_S**, just performs a TV-L^2 denoising of this result [WG13], while **EPI_G** employs a globally optimal labeling scheme [WG12]. Finally, the method **EPI_C** performs a constrained denoising on each epipolar plane image, which takes into account occlusion ordering constraints [GW13].

lightfield	EPI_L	EPI_S	EPI_C	EPI_G	ST_AV_L	ST_AV_S	ST_AV_G	ST_CH_L	ST_CH_S	ST_CH_G
buddha	0.81	0.57	0.55	0.62	1.20	0.78	0.90	1.01	0.67	0.80
buddha2	1.22	0.87	0.87	0.89	2.26	1.05	0.68	3.08	1.31	0.75
horses	3.60	2.12	2.21	2.67	5.29	1.85	1.00	6.14	2.12	1.06
medieval	1.69	1.15	1.10	1.24	7.22	0.91	0.76	12.14	1.08	0.79
mona	1.15	0.90	0.82	0.93	2.25	1.05	0.79	2.28	1.02	0.81
papillon	3.95	2.26	2.52	2.48	4.84	2.92	3.65	4.85	2.57	3.10
stillLife	3.94	3.06	2.61	3.37	5.08	4.23	4.04	4.48	3.36	3.22
couple	0.40	0.18	0.16	0.19	0.60	0.24	0.30	1.10	0.24	0.30
cube	1.27	0.85	0.82	0.87	1.28	0.51	0.56	2.25	0.51	0.55
maria	0.19	0.10	0.10	0.11	0.34	0.11	0.11	0.51	0.11	0.11
pyramide	0.56	0.38	0.38	0.39	0.72	0.42	0.42	1.30	0.43	0.42
statue	0.88	0.33	0.29	0.35	1.56	0.21	0.21	3.39	0.29	0.21
average	1.64	1.07	1.04	1.18	2.72	1.19	1.12	3.54	1.14	1.01

Figure 7: *Detailed evaluation of all disparity estimation algorithms described in section 4 on all of the data sets in our benchmark. The values in the table show the mean squared error in pixels times 100, i.e. a value of "0.81" means that the mean squared error in pixels is "0.0081". See text for a discussion.*

4.1.2. Multi-view stereo

We compute a simple local stereo matching cost for a single view as follows. Let $V = \{(s_1,t_1),...,(s_N,t_N)\}$ be the set of N view points with corresponding images $I_1,...,I_N$, with (s_c,t_c) being the location of the current view I_c for which the cost function is being computed. We then choose a set Λ of 64 disparity labels within an appropriate range. For our test we choose equidistant labels within the ground truth range for optimal results. The local cost $\rho_{\mathrm{AV}}(x,l)$ for label $l \in \Lambda$ at location $x \in I_c$ computed on *all* neighbouring views is then given by

$$\rho_{\mathrm{AV}}(x,l) := \sum_{(s_n,t_n)\in V} \min(\varepsilon, \|I_n(x+lv_n) - I_c(x)\|), \qquad (3)$$

where $v_n := (s_n - s_c, t_n - t_c)$ is the view point displacement and $\varepsilon > 0$ is a cap on the error to suppress outliers. To test the influence of the number of views, we also compute a cost function on a "crosshair" of view points along the s- and t-axis from the view (s_c,t_c), which is given by

$$\rho_{\mathrm{CH}}(x,l) := \sum_{\substack{(s_n,t_n)\in V \\ s_n=s_c \text{ or } t_n=t_c}} \|I_n(x+lv_n) - I_c(x)\|. \qquad (4)$$

In effect, this cost function thus uses exactly the same number of views as required for the local structure tensor of the center view. The results of these two purely local methods can be found under **ST_AV_L** for all views, and **ST_CH_L** for all views or just a crosshair, respectively.

Results of both multiview dataterms are denoised with a simple TV-L^2 scheme, algorithms **ST_AV_S** and **ST_CH_S**. Finally, they were also integrated into a global energy functional

$$E(u) = \int_\Omega \rho(x,u(x))\,\mathrm{d}x + \lambda \int_\Omega |Du| \qquad (5)$$

for a labeling function $u : \Omega \to \Lambda$ on the image domain Ω, which is solved to global optimality using the method in [PCBC10]. The global optimization results can be found under algorithms **ST_AV_G** and **ST_CH_G**.

4.1.3. Results and discussion

At the moment of writing, the most accurate method over all data sets is the straight-forward global stereo ST_CH_G. Interestingly, using only a subset of input views gives more accurate results after global optimization, while the data term accuracy is clearly worse. However, global stereo takes several minutes to compute. Among the real-time capable methods, EPI_S and the ST_S methods perform comparably well. The difference is that the stereo methods only compute the disparity map for the center view in real-time, while EPI_S recovers disparity for all views simultaneously, which might be interesting for further processing. Furthermore, EPI_S and EPI_C do not discretize the disparity space, so accuracy is independent of computation time.

As usual, overall performance depends very much on parameter settings, for the results here, we did a parameter search to find the optimum for all methods on each data set separately. In the future, we would like to do a second run with equal parameter values for each data set, which might turn out quite interesting. These results will also be available online.

4.2. Multiple layer estimation

One of our data sets is special in that it contains a transparent surface, so there are two disparity channels, one for the transparent surface and one for the object behind it, see figure 3. For this case, we currently only have one method implemented [Ano13], and we are quite interested in whether it can be done better.

4.3. Light field labeling algorithms

For labeling, we have implemented all algorithms which are described in [WSG13]. The results are equivalent, and we refer to this work for details. Test scripts to re-generate all their results are included with the source code.

5. Conclusion

We have introduced a new benchmark database of densely sampled light fields for the evaluation of light field analysis algorithms. The database consists of two categories. In the first category, there are artificial light fields rendered with Blender [Ble], which provide ground truth disparities for all views. For some of those light fields, we additionally provide ground truth labels for object segmentation. In the second category, there are real-world scenes captured using a single camera mounted on a gantry, for which we provide (partial) ground truth disparity data for the center view, generated via fitting a mesh from a structured light scan to the views. A large contribution is the source code for an extensive evaluation of reference algorithms from multi-view stereo, epipolar plane image analysis and segmentation on the entire database.

The paper only describes a current snapshot for the database, and explains only a subset of the available source code, which offers many more optimization models and data terms. Both will be regularly updated, in particular we plan new light fields recorded with a plenoptic camera and with available ground truth depth data, as well as extensions of the code base with reference implementations of more multi-view reconstruction algorithms.

6. Acknowledgement

We thank Julie Digne from the LIRIS laboratory of the Claude-Bernard University for providing multiple of the scanned objects. We also thank Susanne Krömker from the Visualization and Numerical Geometry Group of the IWR, University of Heidelberg as well as the Heidelberg Graduate School of Mathetmatical and Computational Methods for the Sciences (HGS MathComp) for providing us with high precission 3D scans and support.

References

[AB91] ADELSON E., BERGEN J.: The plenoptic function and the elements of early vision. *Computational models of visual processing 1* (1991). 1

[Ano13] ANONYMOUS: Anonymous. In *under review* (2013). 7

[BBM87] BOLLES R., BAKER H., MARIMONT D.: Epipolar-plane image analysis: An approach to determining structure from motion. *International Journal of Computer Vision 1*, 1 (1987), 7–55. 6

[Ble] Blender Foundation. `www.blender.org`. 2, 8

[Bra00] BRADSKI G.: The OpenCV Library. *Dr. Dobb's Journal of Software Tools* (2000). 5

[CKS*05] CRIMINISI A., KANG S., SWAMINATHAN R., SZELISKI R., ANANDAN P.: Extracting layers and analyzing their specular properties using epipolar-plane-image analysis. *Computer vision and image understanding 97*, 1 (2005), 51–85. 6

[EM03] ESEDOGLU S., MARCH R.: Segmentation with Depth but Without Detecting Junctions. *Journal of Mathematical Imaging and Vision 18*, 1 (2003), 7–15. 2

[GW13] GOLDLUECKE B., WANNER S.: The Variational Structure of Disparity and Regularization of 4D Light Fields. In *Proc. International Conference on Computer Vision and Pattern Recognition* (2013). 6

[KSS12] KOWDLE A., SINHA S., SZELISKI R.: Multiple View Object Cosegmentation using Appearance and Stereo Cues. In *Proc. European Conference on Computer Vision* (2012). 2

[KZ02] KOLMOGOROV V., ZABIH R.: Multi-camera Scene Reconstruction via Graph Cuts. In *Proc. European Conference on Computer Vision* (2002), pp. 82–96. 6

[LH96] LEVOY M., HANRAHAN P.: Light field rendering. In *Proc. SIGGRAPH* (1996), pp. 31–42. 1

[LNA*06] LEVOY M., NG R., ADAMS A., FOOTER M., HOROWITZ M.: Light field microscopy. *ACM Transactions on Graphics (TOG) 25*, 3 (2006), 924–934. 1

[Ng06] NG R.: *Digital Light Field Photography*. PhD thesis, Stanford University, 2006. Note: thesis led to commercial light field camera, see also `www.lytro.com`. 1

[PCBC10] POCK T., CREMERS D., BISCHOF H., CHAMBOLLE A.: Global Solutions of Variational Models with Convex Regularization. *SIAM Journal on Imaging Sciences* (2010). 7

[PW10] PERWASS C., WIETZKE L.: The Next Generation of Photography, 2010. `www.raytrix.de`. 1

[SHH07] STEIN A., HOIEM D., HEBERT M.: Learning to Find Object Boundaries Using Motion Cues. In *Proc. International Conference on Computer Vision* (2007). 2

[The10] THE HDF GROUP: Hierarchical data format version 5, 2000-2010. URL: `http://www.hdfgroup.org/HDF5`. 2

[WG12] WANNER S., GOLDLUECKE B.: Globally consistent depth labeling of 4D light fields. In *Proc. International Conference on Computer Vision and Pattern Recognition* (2012), pp. 41–48. 4, 6

[WG13] WANNER S., GOLDLUECKE B.: Variational Light Field Analysis for Disparity Estimation and Super-Resolution. *IEEE Transactions on Pattern Analysis and Machine Intelligence* (2013). 6

[WJV*05] WILBURN B., JOSHI N., VAISH V., TALVALA E.-V., ANTUNEZ E., BARTH A., ADAMS A., HOROWITZ M., LEVOY M.: High performance imaging using large camera arrays. *ACM Transactions on Graphics 24* (July 2005), 765–776. 1

[WSG13] WANNER S., STRAEHLE C., GOLDLUECKE B.: Globally Consistent Multi-Label Assignment on the Ray Space of 4D Light Fields. In *Proc. International Conference on Computer Vision and Pattern Recognition* (2013). 2, 4, 8